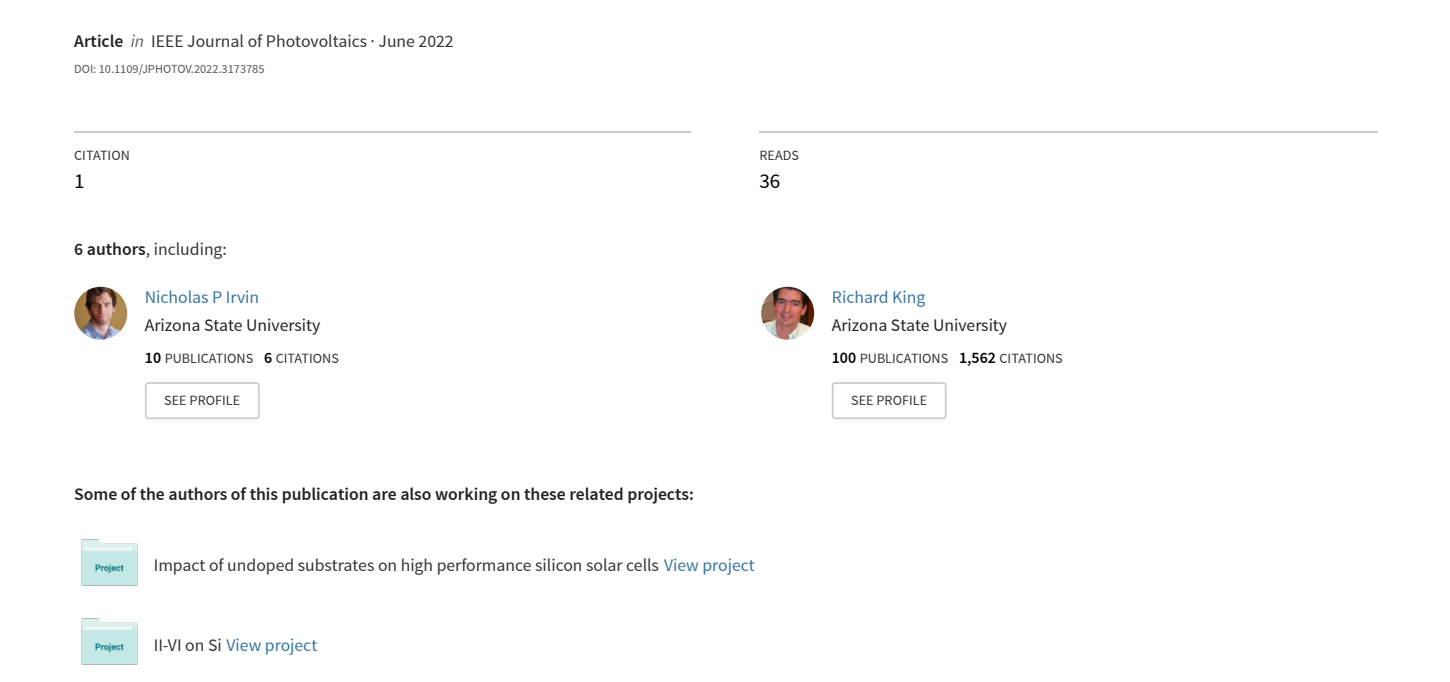
Thermal Impact of Rear Insulation, Light Trapping, and Parasitic Absorption in Solar Modules



Thermal Impact of Rear Insulation, Light Trapping, and Parasitic Absorption in Solar Modules

Nicholas P. Irvin, *Graduate Student Member, IEEE*, D. Martínez Escobar,
Aaron Wheeler, *Graduate Student Member, IEEE*, Richard R. King, *Fellow, IEEE*, Christiana B. Honsberg, and Sarah R. Kurtz, *Fellow, IEEE*

Abstract—Reflection of sub-bandgap light has been argued to be the most effective path to lower temperature solar modules. This report compares GaAs modules with high sub-bandgap reflection to various Si modules under two experimental thermal configurations. At one sun, the GaAs modules operate ~6 °C colder than both multicrystalline and monocrystalline Si within an open-rack configuration. This thermal advantage increases to \sim 13 °C for the thermally insulated configuration. The experimental data are used to build a theoretical model, finding agreement with root-mean-square error between 1.4°C-2.8 °C. The model shows the main thermal advantage of these GaAs modules to be their high sub-bandgap reflection of 79%. Next, it is shown that the sub-bandgap reflection in modules with textured Si cells is fundamentally limited compared to values achieved by the planar GaAs modules, because of the amplification of parasitic absorption that occurs with light trapping. In Si modules, light trapping more than doubles the parasitic absorption of encapsulation layers, limiting the maximum sub-bandgap reflection to 63%. Higher values require thorough optimization of front, bulk, and rear layers, but could lower operating temperatures by up to 12 °C for insulated Si modules.

Index Terms—Building-integrated photovoltaics, gallium arsenide, light trapping, PV modules, silicon, sub bandgap reflection, thermal management, vehicle-integrated photovoltaics.

I. INTRODUCTION

RECENTLY, solar panels have been deployed in a growing variety of thermal configurations. While standard test conditions (STC) consider module temperatures to be 25 °C, vehicle-integrated solar can face temperatures over 85 °C [1]. Such temperatures can occur when an insulated rear surface reduces overall cooling. Insulated configurations, thus, run hotter than conventional open-rack configurations, where modules

Manuscript received December 20, 2021; revised March 15, 2022; accepted April 5, 2022. This work was supported in part by the Engineering Research Center Program of the National Science Foundation (NSF) and in part by the Office of Energy Efficiency and Renewable Energy of the Department of Energy under NSF Cooperative Agreement under Grant EEC-1041895. (Corresponding author: Nicholas P. Irvin.)

Nicholas P. Irvin, Richard R. King, and Christiana B. Honsberg are with the Arizona State University, Tempe, AZ 85281 USA (e-mail: npirvin93@gmail.com; richard.r.king@asu.edu; Christiana.Honsberg@asu.edu)

D. Martínez Escobar, Aaron Wheeler, and Sarah R. Kurtz are with the University of California Merced, Merced, CA 95343 USA (e-mail: maeddalia@gmail.com; awheeler6@ucmerced.edu; skurtz@ucmerced.edu).

Color versions of one or more figures in this article are available at https://doi.org/10.1109/JPHOTOV.2022.3173785.

Digital Object Identifier 10.1109/JPHOTOV.2022.3173785

benefit from rear convective and radiative cooling. Buildingintegrated photovoltaics lie between open-rack and fully insulated configurations, depending on ventilation [2].

The higher temperatures faced in insulated configurations generally reduce module efficiency [3]. Crystalline silicon experiences a greater loss in efficiency with temperature than amorphous Si (a-Si), CdTe, and GaAs [4]. GaAs, the core material for space applications [5], is very expensive but offers multiple performance advantages over Si. These advantages include higher power density, lower sensitivity to module temperature, and lower module operating temperatures. The two main effects causing lower operating temperatures in GaAs modules are a high photovoltaic efficiency [6] and a high sub-bandgap reflectance [7].

Sub-bandgap reflection has been shown to be a particularly effective way to lower module temperatures [7]–[10]. This article builds on previous work by quantifying the effect of sub-bandgap reflection, convection, and radiative cooling in two thermal configurations, yielding projected performance differences for a range of conditions and climates. This article also clarifies the impact of light trapping on sub-bandgap reflectance and module temperature. Section II details the experimental and modeling methods. Then, Section III-A compares photovoltaic performance across thermal configurations. Finally, Section III-B examines fundamental limitations and practical benefits of sub-bandgap reflection for Si modules.

II. METHODS

A. Experimental Design

The experimental apparatus, depicted in Fig. 1, puts six solar modules into one of two thermal configurations: the open-rack or insulated configuration.

In the insulated configuration, the rear is covered with 10 cm of fiberglass batt, which is held up by plywood. In the open-rack configuration, the rear backsheet is exposed to the air and ground below. All modules were connected to the structure using insulating material to isolate them from the frame and racking. The mounting structure is 2.4 m \times 2.4 m in area and mounted 1 m above ground. The surface has a 5° tilt due south to allow rainwater to run off.

The outdoors test facility is installed at Merced, CA, 37.3746 ° N, -120.5788 ° W, and 58 m elevation. The solar panels are mounted flush with the black-anodized aluminum

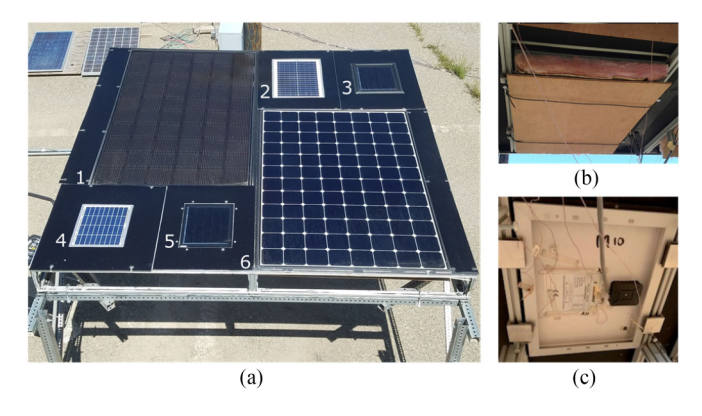


Fig. 1. (a) Photograph of the experimental rack with two single-crystal Si modules (1, 6), two multicrystalline Si modules (2, 4), and two GaAs modules (3, 5). At different test times, the back surfaces of the modules are either insulated with fiberglass batt (b) or open from backsheet to the ground (c).

sheet seen in Fig. 1. The modules include two single-crystal Si modules (SC-Si), two multicrystalline Si modules (MC-Si), and two thin-film GaAs modules. A variety of Si modules were chosen for a range of efficiencies and sub-bandgap reflectances.

Modules were biased at their maximum power point with data logged every three minutes on a Daystar MT5 multitracer. Current-voltage measurements were acquired every five minutes but were not used in this article. Temperatures were measured with T-type thermocouples attached to the center of module backsheets using glass cloth electrical tape (Scotch series 27). An in-plane thermopile pyranometer records irradiance, while a cup anemometer records wind speed and direction. An Omega HX71-V2 sensor recorded relative humidity. The daytime average was 35%.

B. Theoretical Model

The module temperature is calculated through the thermal balance equation [11]

$$AG = h_{cf} \cdot (T_{mod} - T_{amb}) + \varepsilon_{g} \cdot (\sigma T_{mod}^{4} - R_{sky})$$
$$+ \delta_{cf} \varepsilon_{b} \sigma \cdot (T_{mod}^{4} - T_{gnd}^{4}) + \eta (G)$$
(1)

where A is the module's full-spectrum absorptance, G is the solar irradiance in W/m², $h_{\rm cf}$ is the module's convection coefficient within each configuration, $T_{\rm mod}$ is the module temperature in K, $T_{\rm amb}$ is the ambient temperature, $\varepsilon_{\rm g}=0.84$ is the emissivity of glass while $\varepsilon_{\rm b}=0.893$ is the backsheet's emissivity [11], σ is the Stefan-Boltzmann constant, $T_{\rm gnd}$ is the ground temperature, and η is the photovoltaic efficiency with respect to the total cell area. $\delta_{\rm cf}$ is 0 in the insulated configuration and is 1 in the open-rack configuration, as rear radiation only occurs in the open-rack configuration. G, $T_{\rm mod}$, $T_{\rm amb}$, $T_{\rm gnd}$, and the maximum power were remeasured every three minutes. $R_{\rm sky}$, the sky's thermal downwelling radiation, is found by inputting humidity and ambient temperature into the model fit (4) from [12]. For data with direct measurements, the efficiency η is calculated from the measured power.

To extrapolate the model to different cities, inputs including irradiance, ambient temperature, and wind speed are taken from typical meteorological year data. Variation in efficiency with temperature is incorporated with the substitution $\eta=$

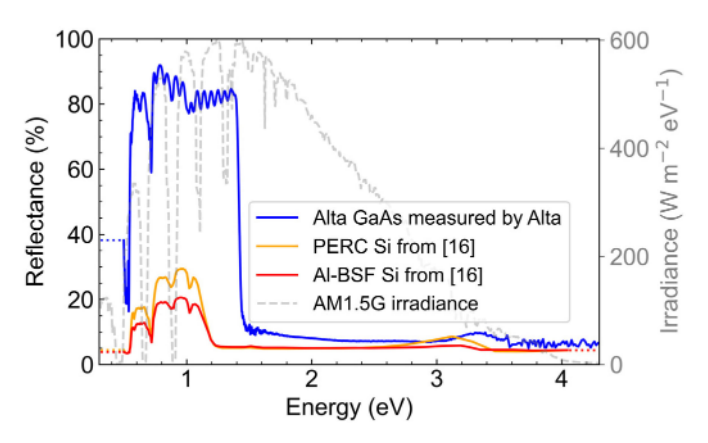


Fig. 2. Measured reflectance of encapsulated modules, showing a much higher sub-bandgap reflectance for GaAs.

 $\begin{tabular}{l} TABLE I \\ Full-Spectrum Absorptance A \end{tabular}$

GaAs	SC-Si	MC-Si
0.658	0.909	0.923

 $\eta_{\rm STC}$ $(1+\gamma[T_{\rm mod}-25\,^{\circ}{\rm C}])$ into (1), which is then solved numerically to acquire $T_{\rm mod}$. The temperature coefficients γ are taken from previously reported measurements on these modules [13]. The STC efficiency $\eta_{\rm STC}$ was extracted using a linear fit to extrapolate to 25 °C while simultaneously filtering the data for irradiances near 1000 W/m² [13]. The efficiency relative to STC efficiency, defined by $\eta_{\rm rel}=\eta/\eta_{\rm STC}$, is considered to isolate the effects of temperature on performance. The performance ratio is an irradiance-weighted average of the relative efficiency over a year. The module-level performance ratio in this report considers the effects of temperature but not of soiling, shadowing, inverter, or other system-level issues [14].

The value of A, the full absorptance of all layers in the active area, is found once for each module from

$$A(E) = \frac{\int (1 - R(E))G_{AM}(E) dE}{\int G_{AM}(E) dE}$$
 (2)

where R is the reflectance as a function of photon energy, E, and $G_{\rm AM}$ is the spectral irradiance (W·m⁻²·eV⁻¹) taken from the AM1.5G solar standard [15]. Integration is done across the tabulated AM1.5G energy range of 0.31–4.43 eV. The reflectance curves for encapsulated modules are given in Fig. 2, showing high reflection for energies below the bandgaps, which are 1.125 eV for Si and 1.424 eV for GaAs. The GaAs sub-bandgap reflectance shows substantial improvement over modules used in [6]. Nevertheless, parasitic absorption in the encapsulant reduces sub-bandgap reflection at specific energies, including 0.72 eV.

The GaAs reflectance curves were measured directly with an Agilent Cary spectrophotometer by Alta Devices Inc. The Si curves are taken from experiments of [16]. For the high-efficiency, single-crystal Si, we use the passivated emitter and rear contact (PERC) reflectance with line contacts. For the multicrystalline modules, we use the aluminum back-surface field (Al-BSF) reflectance. The calculated A values are given by Table I.

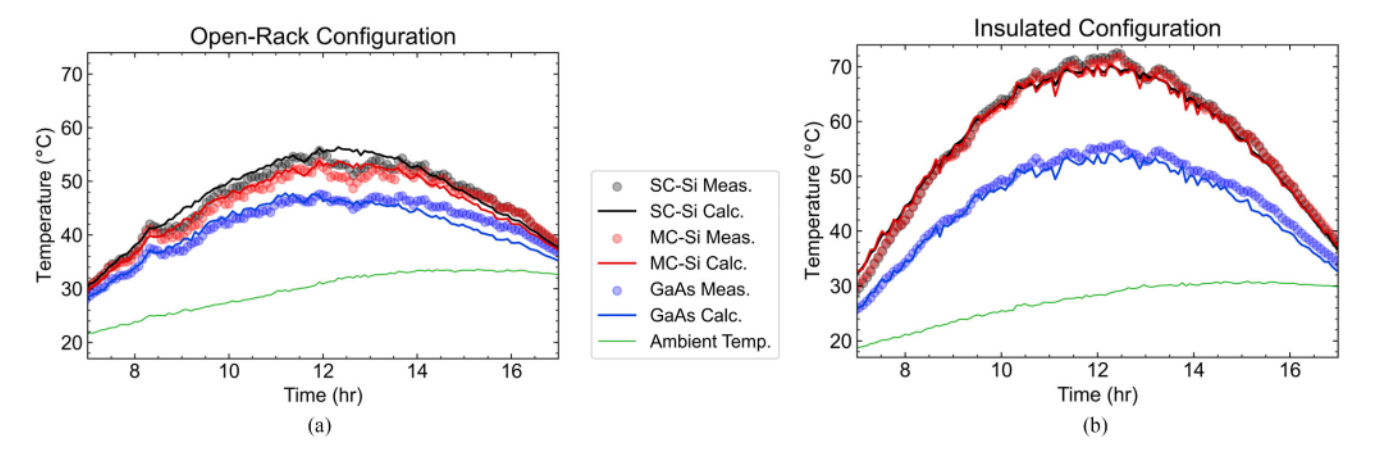


Fig. 3. Module temperatures for the (a) open-rack and the (b) insulated configurations for two days during mid-summer in Merced, CA. In the insulated configuration, the Si module temperatures, MC-Si1 and SC-Si2, are seen to be much greater than those of GaAs1. Calculations match measured values within an rms error of 1.4–2.8 °C for each module over multiple months.

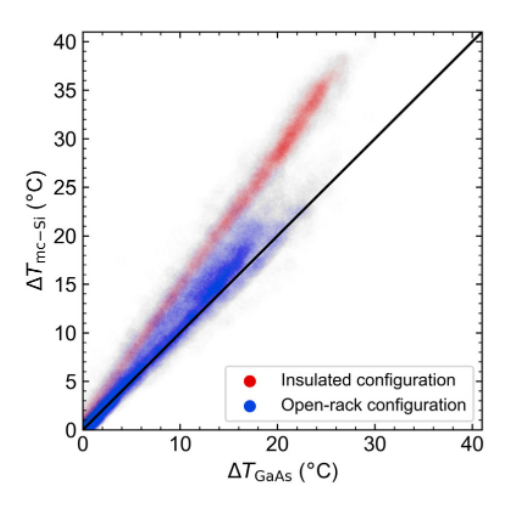


Fig. 4. Comparison of measured ΔT (module temperature above ambient) over several months for GaAs1 and MC-Si2.

The reflection measurements span only part of the AM1.5G spectrum, so they were extended to the spectrum's limits through a constant-value extrapolation, as shown with the dotted segments in Fig. 2. The limited measurement range creates a small amount of uncertainty. For GaAs, A changes from 0.658 to 0.665 if the extrapolated reflectance values are replaced with 0%, and changes to 0.651 if they are replaced with 100%. For SC-Si, the possible range for A is 0.898-0.910, and, for MC-Si, it is 0.912-0.924.

The final parameter, the convection coefficient $h_{\rm cf}$, is found by fitting (1) across the set of measurements for each module under the insulated configuration. Results extend to the openrack configuration according to

$$h_{\rm cf} = \left[\left(h_1 * v + h_2 \right)^3 + h_3^3 \right]^{1/3} + \delta_{\rm cf} h_3 \tag{3}$$

where v is the wind speed and $\delta_{\rm cf}$ is 0 or 1 for the insulated or open-rack configuration, respectively. Allowing for different convection coefficients $(h_1, h_2, \text{ and } h_3)$ for each module reduces root-mean-square (rms) error between model and measurement by 30%. The fitted values are given in Table II.

TABLE II $\label{eq:table_entropy} \text{Fitted Convection Coefficients } (W\ M^{-2}\ K^{-1})$

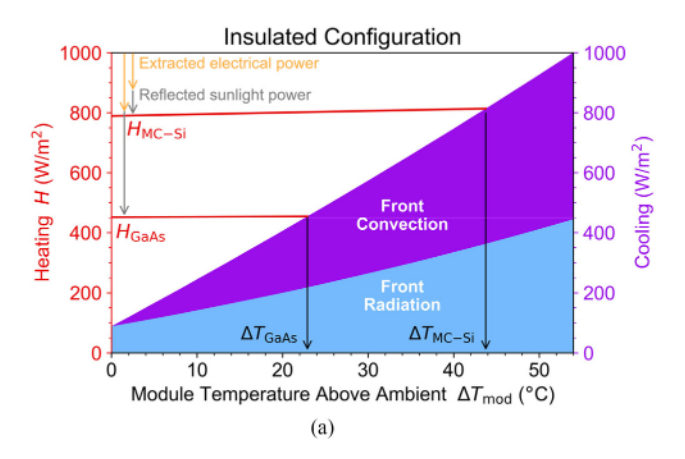
	GaAs1	GaAs2	MC- Si1	MC- Si2	SC- Si1	SC- Si2
h_1	2.9	2.5	3.6	4.1	1.4	0.8
h_2	0.88	0	0.14	2.2	6.3	6.4
h_3	6.8	5.8	9.1	12	4.6	4.7

The convection coefficients are uncertain because the fitting can compensate for inaccuracy in any modeling parameter with an underestimate or overestimate in a convection coefficient. For example, if the glass emissivity of 0.84 taken from [11] is replaced with the value of 0.91 quoted in [17], GaAs1's fitted convection coefficients change to 2.6, 0.9, and 5.9, which reduces the effective convection coefficient h_{cf} by about 12%. Nonetheless, the fitted values are reasonable. The forced-convection values $h_1 * v + h_2$ align closely with models of [18]–[20]. The fitted natural-convection coefficient h_3 can be compared to the theory of [17], which calculates the coefficient based on the characteristic dimension of the surface. That dimension itself is made uncertain by the presence of the large mounting rack, leading to upper and lower bounds for h_3 . These bounds are satisfied, as the fitted h_3 values lie between the values calculated from the geometry of the whole rack (2.8 W/(m²·K)) and from the geometry of the module alone [ranging 4.6–14.6 W/(m²·K)]. Finally, the resultant h_{cf} values are smallest for the largest-area modules and are biggest for the modules positioned at the rack's corners, which can be expected as air is colder at the rack's edge than its center.

III. RESULTS

A. Effect of Thermal Configurations

Before using the model for explanatory results, it is assessed by comparing calculated and measured temperatures. The curves match quite well, as seen in Fig. 3 for a representative summer day. Calculations match measurements with rms errors within



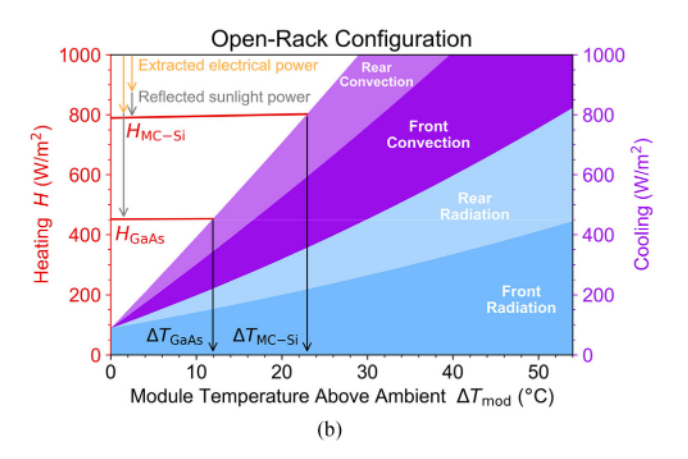
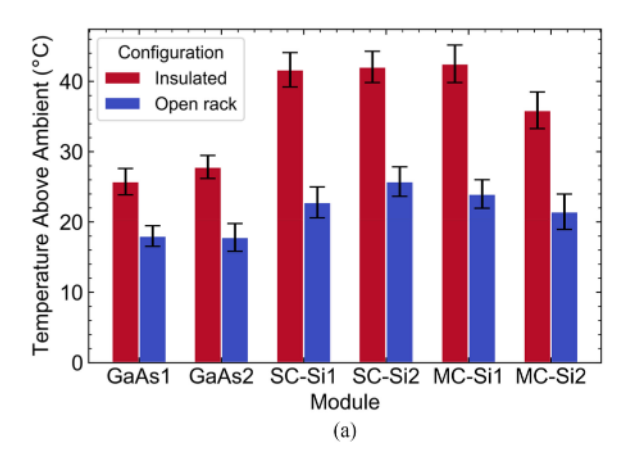


Fig. 5. Depiction of thermal balance for modules in (a) insulated configuration and (b) open-rack configuration. The data are calculated for 1000 W/m² irradiance, 1.9 m/s wind speed, and 25 °C ambient and ground temperatures. GaAs modules are seen to run colder primarily through higher sub-bandgap reflectance. The impact of sub-bandgap reflection leads to greater temperature differences in the insulated configuration.



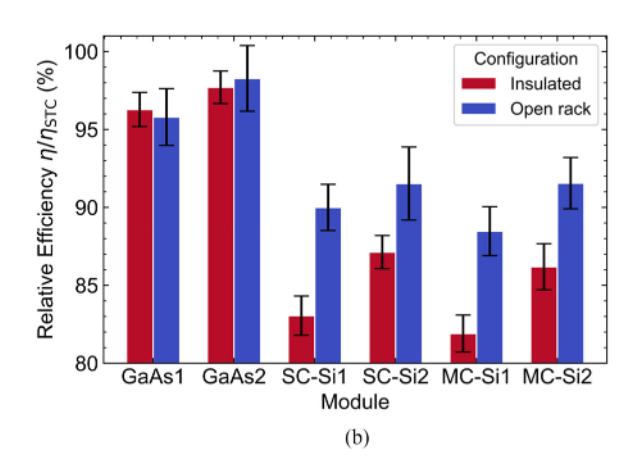


Fig. 6. Experimental (a) module temperature and (b) relative efficiency (relative to STC efficiency) of GaAs, multicrystalline Si, and single-crystal Si. The data are filtered for weather around 30 °C ambient and 1000 W//m² irradiance. The insulated configuration creates hotter temperatures for all modules. The silicon efficiencies are greater in the open-rack than insulated configuration, but the GaAs efficiencies are practically independent of thermal configuration.

2.8 °C for each module in the open rack configuration. The rms error reduces to 1.4 °C for insulated GaAs modules.

The thermal advantage of GaAs can also be seen in Fig. 3. On the day shown, GaAs operates up to 8.2 °C cooler than Si in the open-rack configuration—compared to 16.9 °C cooler in the insulated configuration. One may expect the temperature difference to be larger in the insulated configuration as temperatures are magnified by lower cooling.

Fig. 4 compares the increase of module temperatures above ambient temperature ΔT for Si and GaAs modules across several months of data. The ratio $\Delta T_{\rm Si}/\Delta T_{\rm GaAs}$ is greater in the insulated configuration. In the insulated configuration $\Delta T_{\rm Si}/\Delta T_{\rm GaAs}$ stays near 1.4, while the open-rack ratio varies from 0.9 to 1.3. This variation in the ratio is partly due to movement of the rack's shadow; when the rack shadows the ground beneath the module, the module receives less radiative heat from the ground. Another reason for the varying ratio is nonlinearity in the radiation terms—as can be seen in Fig. 5.

Fig. 5 depicts the thermal balance for MC-Si1 and GaAs1. Modules are graphed on one plot by using only $h_{\rm cf}$ of GaAs1. Balance of the heating load with convective and radiative cooling

determines the module temperature. The heating load is reduced by reflection and electrical extraction, as shown in Fig. 5. The temperature dependence of the extracted power, -0.05%/°C for GaAs and -0.42%/°C for MC-Si, leads to only a slight variation in each heat load across the *x*-axis (i.e., the red lines are not horizontal). The difference between the heat loads of the two modules, however, is significant. The heat load of GaAs is much lower than that of Si *primarily due to higher reflection* and secondarily to greater extraction. Comparison of Fig. 5(a) and (b) shows that the cooling effect of sub-bandgap reflection becomes magnified in the insulated configuration. In the open-rack configuration, both modules run cooler due to rear convection and rear radiation.

Fig. 6 presents a statistical summary of the experimental results, giving averages and standard deviations for module temperature and relative efficiency. To isolate them from changes in the weather, the data have been filtered for irradiances between 900–1050 W/m², wind speeds 0.5–1.5 m/s, and ambient temperatures 25–35 °C. Fig. 6(a) shows that GaAs modules run significantly cooler than Si—especially in the insulated configuration. The temperature difference between silicon module

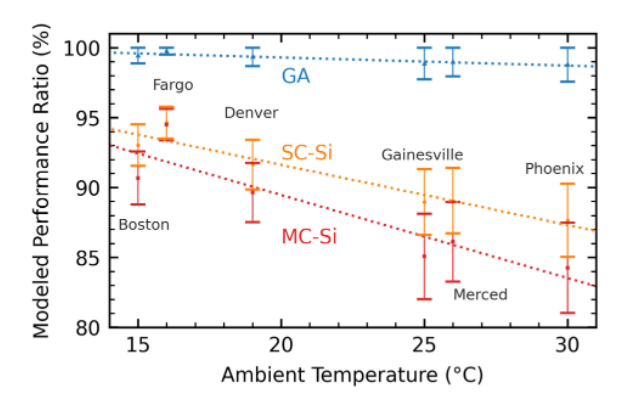


Fig. 7. Module-level performance ratio showing the effect of climate on insulated modules. The ambient temperature largely determines the modeled performance loss, while wind and humidity introduce some scatter to a linear fit.

types is within the experimental uncertainty. The impact of configuration on relative efficiency is given in Fig. 6(b). The Si modules operate much more efficiently in the cooler open-rack configuration, but the GaAs performance appears independent of configuration. This result demonstrates extra power in using GaAs for insulated applications.

The experiments were in Merced, CA—a relatively warm locale. The model is used to extrapolate results to various cities, plotted in Fig. 7 against irradiance-averaged ambient temperature. The performance losses due to temperature are nearly three times as large in Phoenix, AZ as in Fargo, ND. Although weather conditions such as irradiance, wind speed, and humidity are considered in Fig. 7, the ambient temperatures largely determine the performance loss of hot modules.

Error bars in Fig. 7 indicate the difference between temperature coefficients found from indoor and outdoor measurements [13]. Although the MC-Si and SC-Si modules operate at similar temperatures, the MC-Si are expected to receive a greater performance loss due to a steeper temperature coefficient. In insulated configurations, the MC modules can lose 16% of their efficiency relative to STC. These results motivate redesigning Si modules to operate at cooler temperatures for insulated configurations.

B. Enhancement of Sub-Bandgap Reflection

Sub-bandgap reflection can significantly reduce a module's heat input. However, the effective sub-bandgap reflectance for commercial Si modules has been measured as 15–21%—values far below optimal [16]. The sub-bandgap reflectance $R_{\rm sub}$ can be derived through ray tracing [21] or conservation methods [22]. For planar modules without light scattering

$$R_{\text{sub}} = R_{\text{ext}} + \frac{(1 - R_{\text{ext}}) R_{\text{b}} T_{\text{ps}}^2 T_{\text{pf}}^2 (1 - R_{\text{int}})}{1 - R_{\text{b}} T_{\text{ps}}^2 T_{\text{pf}}^2 R_{\text{int}}}$$
(4)

where $R_{\rm ext}$ is the external front reflectance, $R_{\rm int}$ is the internal front reflectance, and $R_{\rm b}$ is the back-surface reflectance. $T_{\rm ps}$ and $T_{\rm pf}$ are the transmittances of light through the semiconductor layers and front encapsulation layers, respectively. Transmittance is calculated as the product of ${\rm e}^{-W~\alpha(E)}$ for each layer, where W is the layer thickness and α the absorption coefficient. The transmittances and the sub-bandgap reflection are considered as a function of energy E.

Sub-bandgap reflection depends strongly on parasitic absorption (PA) [22], [23]. The tabulated absorption coefficients for PA in encapsulation materials are taken from [24]. The encapsulant, typically ethylene vinyl acetate (EVA), has a relatively high absorption at energies 1.02, 0.88, 0.72, 0.56 eV, and below, leading to the reflectance minima in Fig. 2. Experimental reports have shown EVA encapsulation to reduce sub-bandgap reflection of point-contact PERC cells by 34% relative to bare cells [16].

The analysis in this section will calculate parasitic absorption in the glass, encapsulant, and silicon emitter and base layers. Losses to the rear will be parametrized by the reflectance of the back surface (a variable that depends on the Si-Al alloy in the case of Al-BSF and on the dielectric/Al grid in the case of PERC). The encapsulation is taken as 0.4 mm thick and the soda-lime glass as 3.2 mm. PA in Si layers is modeled with free carrier absorption [25]. For a p-type 180 μ m base, the hole concentration is taken as 7.6·10¹⁵ cm⁻³, characteristic of PERC [26]. For an n-type 0.7 μ m emitter, the electron concentration is modeled through an integration over one of two Gaussian doping profiles. A moderate-doping profile with a maximum of $2 \cdot 10^{20}$ cm⁻³ and a total dose of 10^{15} cm⁻² represents a typical commercial profile, which is used to compare calculations to experimental values [27]. Alternatively, a low-doping profile with a maximum of $9 \cdot 10^{18}$ cm⁻³ and a total dose of 10^{14} cm⁻² is later used to represent the level that can be achieved through selective emitters [27]. The effect of doping on the photovoltaic efficiency is not considered (except through the efficiency's temperature dependence).

For textured cells, the thicknesses W are scaled by two due to the longer path when light scatters into oblique angles (at an average of 60° for Lambertian scattering) [28]. Light refraction will also cause some photons (around 10% per pass) to transmit from Si into the encapsulation materials before reflecting at the glass/air interface. So, for modules with textured cells

$$R_{\text{sub}} = R_{\text{ext}} + \frac{(1 - R_{\text{ext}}) R_{\text{b}} T_{\text{ps}}^2 T_{\text{pf}}^2 (1 - R_{\text{int}})}{1 - R_{\text{b}} T_{\text{ps}}^2 \left(R_{\text{i1}} + (1 - R_{\text{i1}}) R_{\text{i2}} T_{\text{pf}}^2 \right)}$$
(5)

where $R_{\rm i1}=1-n_2^2/n_1^2$, $R_{\rm i2}=1-1/n_2^2$, $n_1=3.5$ is the index of refraction in Si, and $n_2=1.5$ the index in the encapsulant and glass. (Using energy-dependent indices of refraction would not significantly alter the sub-bandgap reflection.) Si cells are textured to create light trapping, which drastically increases the internal front reflectance $R_{\rm int}$. For ideal texturing, the angle-averaged value becomes $R_{\rm int}=1-1/n_1^2=92\%$ [28]. For planar cells, internal reflection is much smaller: $R_{\rm int}=R_{\rm ext}$. The value $R_{\rm ext}=5\%$ is taken from Si's reflection at 2.5 eV in Fig. 2.

The impact of higher internal front reflection is depicted in Fig. 8(a). Light trapping increases the path length of light in the Si layers to $50 \times W$, which dwarfs the $2 \times W$ experienced by a planar cell with an ideal rear reflector [29]. The longer path increases the chance of parasitic absorption at bulk, rear, and front layers. Due to the intermediate indices of the glass and encapsulant, a fraction of outgoing light will refract into long paths through the encapsulation layers before reflecting at the glass-air interface. Within a Lambertian light distribution (attributed to ideal texturing), the effective path

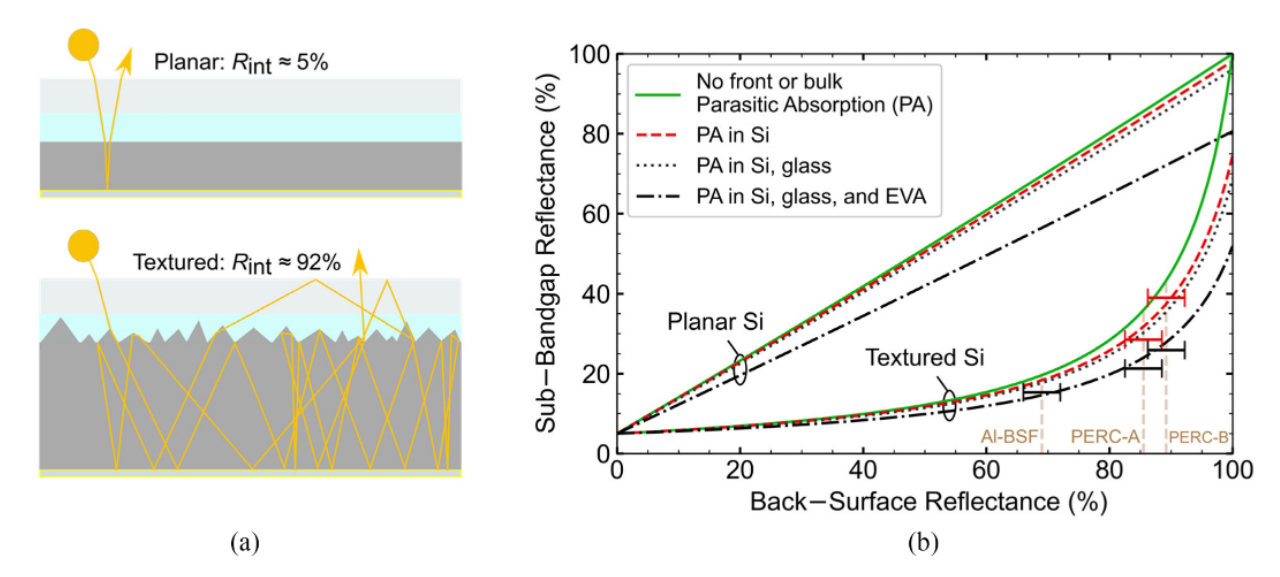


Fig. 8. (a) Illustration of the compounding effect of light trapping on parasitic absorption. Texturing dramatically increases the internal front reflectance $R_{\rm int}$. Thus, sub-bandgap light in textured cells hits interfaces several times more than in planar cells, resulting in more parasitic absorption at front, bulk, and rear layers. (b) Light trapping's effect on the (irradiance-averaged) sub-bandgap reflectance. The sub-bandgap reflectance of textured Si drops precipitously with introduction of parasitic absorption at the front or back. Error bars indicate agreement of calculations with experiments from [16].

 ${\bf TABLE~III}$ Textured Si Sub-Bandgap Reflectance at 100% Rear Reflectance

	Glass & EVA	Glass	Bare
Moderate doping	52.0%	68.8%	74.6%
Low doping	59.9%	82.5%	89.9%
No doping	62.5%	91.5%	100.0%

length through the encapsulation layer increases from $2\times W$ to $8.4\times W$.

Thus, light trapping amplifies the effect of parasitic absorption on $R_{\rm sub}$, leading to the nonlinear curves of Fig. 8(b). The nonlinearity in $R_{\rm b}$ was recently demonstrated in [30].

For modules with textured cells, small deficiencies in backsurface reflection create large drops in sub-bandgap reflection. This sensitivity to the rear reflectance generalizes to various light-trapping geometries [23], although its magnitude depends on the texturing geometry. Texturing also increases sensitivity to PA in semiconductor and encapsulation layers, reducing the maximum sub-bandgap reflectance from 81% to 52% for modules with glass and EVA.

Fig. 8(b) was calculated with the moderate-doping profile to enable comparison of the calculated curves with experimental results from [16]. Indeed, the bare and encapsulated curves here agree with the experimental error bars. The experimental sub-bandgap reflectances were taken from irradiance-weighted averages of bare and encapsulated curves for the Al-BSF, line-contact (PERC-A), and point contact (PERC-B) architectures [16]. The back-surface reflectances were found from [31]–[33].

Table III gives the maximum sub-bandgap reflection for textured Si under varying levels of doping and encapsulation. The table shows that the moderate-doping profile reduces the maximum sub-bandgap reflectance by 25% due to free-carrier absorption. This loss reduces to 10% in the low-doping case. The

impact of glass is seen to be small relative to the encapsulant. The encapsulant EVA drastically limits sub-bandgap reflection, reducing the maximum $R_{\rm sub}$ achievable by 38% absolute.

For GaAs modules, the sub-bandgap reflection would follow the linear trend of the planar curves in Fig. 8(b). Sub-bandgap reflection is less sensitive to parasitic absorption for modules with planar cells. This conclusion is supported by Fig. 2, where the irradiance-averaged $R_{\rm sub}$ for GaAs is 79% compared to Si's 15%–26%. The sub-bandgap reflectance for Si modules was measured at 15% for Al-BSF, 21% for PERC-A, and 26% for PERC-B [16]. The values available for unencapsulated cells are 29% for PERC-A and 39% for PERC-B compared to 92% for GaAs. GaAs cells can fundamentally achieve much higher sub-bandgap reflectances due to the relative insensitivity of planar modules on PA. Here, "planar" indicates the lack of light trapping. If the GaAs cells had a planar front but a textured rear, the sub-bandgap reflectance would be reduced.

While light trapping reduces sub-bandgap reflection, it is interesting to note that it can sometimes have the opposite effect on radiative cooling, as increased absorption is associated with increased emissivity and decreased reflection (note, however, that emission of thermal radiation and reflection of sunlight occur largely in different wavelength intervals). The texturing of glass has been shown to increase the emissivity of encapsulated modules [34]. The texturing of silicon layers has been shown to increase the emissivity of unencapsulated cells—but not encapsulated modules [35]. Light trapping in semiconductor layers does not significantly affect radiative cooling of encapsulated modules (due to the high emissivity of glass over mid-infrared wavelengths), but it does significantly reduce the reflection of incident sunlight.

Next, the thermal impact of a varied sub-bandgap reflection is determined by replacing R(E) with $R_{\rm sub}(E)$ for sub-bandgap energies in a recalculation of (1) and (2). Module temperatures (calculated for 1000 W/m² irradiance, 25 °C ambient, 1 m/s wind speed, and the low-doping profile) are given in Fig. 9.

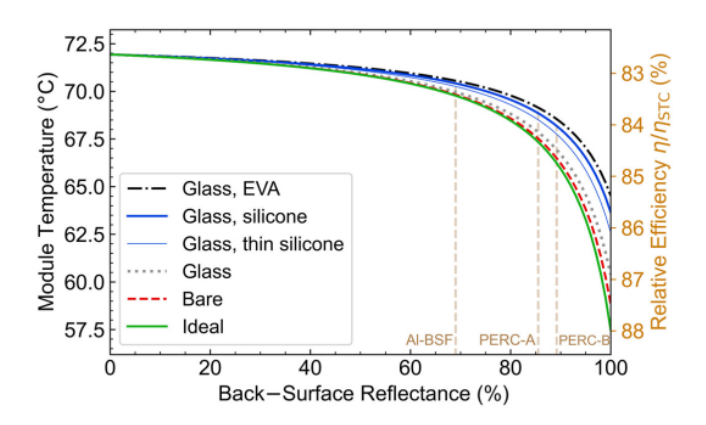


Fig. 9. Cooling due to enhanced reflection of sub-bandgap light for lowly doped SC-Si modules with rear insulation and a 25 °C ambient. Parasitic absorption in the encapsulant severely limits the impact of a higher back-surface reflection.

For bare cells, the results show a potential 12.8 °C reduction from sub-bandgap reflection. Using a temperature coefficient of -0.37%/°C for SC-Si, the efficiency increase is determined as 4.8% relative to STC, which is a 1.0% increase in absolute efficiency. In addition to efficiency, the temperature reduction will likely improve the life span, as module degradation generally increases with temperature [36]–[38].

The ideal curve in Fig. 9 neglects parasitic absorption in encapsulation and semiconductor layers. Although ideal modules can cool by 14.4 °C due to enhanced back-surface reflection, this value drops significantly for encapsulated modules. A module with glass and EVA receives 7.4 °C cooling if its back-surface reflectance improves to 100%. Replacing EVA with the more expensive encapsulant silicone gives marginal benefits in cooling. Using thinner silicone of 0.2 mm would yield some extra benefits—but thinner encapsulants do leave modules more vulnerable to stress-induced damage [39]. The thin silicone encapsulant gives a maximum sub-bandgap reflection of 67%, yielding 9.3 °C cooling.

Substantially more cooling, 11.6 °C, becomes available if PA in the encapsulant could be eliminated. One may consider removing [40] or replacing the encapsulant [41]. A selective filter could be integrated into the glass to reflect sub-bandgap light [7], [42]. The glass itself could be designed as a selective mirror [30], [43]. Perhaps best, a selective filter could be placed between the glass and the encapsulant, which would lower parasitic absorption in the encapsulant while preserving radiative emission from the glass [8].

IV. CONCLUSION

This report compares the value of sub-bandgap reflection across module types and thermal configurations. Multiple configurations were designed to simulate varying thermal scenarios. Across configurations, Si modules ran hotter than the GaAs modules. The temperature difference was highest in the insulated configuration, where cooling factors are reduced. The performance of Si modules in the insulated configuration dropped by several percent relative to the open-rack configuration, but GaAs preserved its high efficiency.

This result demonstrates an extra power advantage in using GaAs over Si for thermally insulated configurations. Although GaAs is too expensive for many large-scale applications, its temperature advantage could become a deciding factor for high-value, small-area applications such as unmanned aerial vehicles or automobile roofs. In addition to reduced power losses, lower temperatures in GaAs likely yield less module degradation. These thermal advantages over c-Si may well extend to other planar thin-film modules such as a-Si, CdTe, CIGS, and perovskites.

The cause of the thermal advantage was determined through a computational model, which was first validated against the measurements. The model explains that the temperature difference derives primarily from the higher sub-bandgap reflection of GaAs and secondarily from its higher photovoltaic efficiency. The GaAs modules reflect 79% of sub-bandgap photons, whereas the various Si modules reflect 15%–26%—resulting in greater heat generation for Si. Enhancing the sub-bandgap reflection of Si could return a quarter of its temperature-induced performance loss—but only if optical properties are highly optimized.

Light trapping amplifies the impact of parasitic absorption, drastically reducing sub-bandgap reflection in modules with textured cells. Thus, modules with textured cells like Si generally require a much higher rear reflectance than planar modules to achieve the same sub-bandgap reflectance. It is shown that light trapping even amplifies parasitic absorption within encapsulation layers. The encapsulant EVA nearly halves the potential value of sub-bandgap reflection for textured Si. Alternative materials for the encapsulant can give marginal improvements—but eliminating parasitic absorption in the encapsulant through advanced designs enables far more benefits. Only then could textured Si achieve the sub-bandgap reflection demonstrated by solar modules with planar, direct bandgap semiconductors like GaAs

Direct bandgap materials, such as GaAs, CdTe, CIGS, a-Si, and perovskites, allow for effective optical absorption without light trapping. By avoiding the heat generation incurred by light trapping, direct bandgap semiconductors become a better fit for applications involving thermal insulation. That thermal advantage would, however, diminish if the direct bandgap materials have light trapping or absorptive rear interfaces. Future studies may seek to quantify the thermal impact of introducing light trapping into specific direct bandgap materials. This impact could be critical to the development of light trapping in perovskites, which have been seen to decompose at temperatures as low as 60 °C [44].

ACKNOWLEDGMENT

The authors would like to thank P. Sims for the reflectance measurements and B. Kayes, M. Limpinsel, and the team at Alta Devices for characterization and fabrication of the GaAs modules, like to thank J. Bryan for stimulating conversations on light management, and also like to thank to P. Sanchez for his support with the data handling.

REFERENCES

- [1] K. McCabe, "Modeling thermal behavior of vehicle integrated photo-voltaics," B.S. thesis, Dept. Mech. Eng., Ohio State Univ., Columbus, OH, USA, 2021. [Online]. Available: https://kb.osu.edu/bitstream/handle/1811/92462/ThesisMcCabe_FinalDraft.pdf?sequence=1&isAllowed=y
- [2] J. J. Bloem, "Evaluation of a PV-integrated building application in a well-controlled outdoor test environment," *Building Environ.*, vol. 43, no. 2, pp. 205–216, Feb. 2008, doi: 10.1016/j.buildenv.2006.10.041.
- [3] J. J. Wysocki and P. Rappaport, "Effect of temperature on photovoltaic solar energy conversion," *J. Appl. Phys.*, vol. 31, no. 3, pp. 571–578, Mar. 1960, doi: 10.1063/1.1735630.
- [4] O. Dupré, R. Vaillon, and M. A. Green, *Thermal Behavior of Photovoltaic Devices: Physics and Engineering*. Berlin, Germany: Springer International Publishing AG, 2017, p. 3, doi: 10.1007/978-3-319-49457-9.
- [5] G. A. Landis, "Review of solar cell temperature coefficients for space," NASA Lewis Research Center, Cleveland, OH, USA, Sep. 1994. Accessed: Aug. 26, 2021. [Online]. Available: https://www.osti.gov/biblio/36446-review-solar-cell-temperature-coefficients-space
- [6] T. J. Silverman et al., "Outdoor performance of a thin-film gallium-arsenide photovoltaic module," in Proc. IEEE 39th Photovolt. Specialist Conf., 2013, pp. 0103–0108, doi: 10.1109/PVSC.2013.6744109.
- [7] T. J. Silverman et al., "Reducing operating temperature in photovoltaic modules," *IEEE J. Photovolt.*, vol. 8, no. 2, pp. 532–540, Mar. 2018, doi: 10.1109/JPHOTOV.2017.2779842.
- [8] X. Sun et al., "Optics-based approach to thermal management of photovoltaics: Selective-spectral and radiative cooling," *IEEE J. Pho*tovolt., vol. 7, no. 2, pp. 566–574, Mar. 2017, doi: 10.1109/JPHO-TOV.2016.2646062.
- [9] R. Vaillon, O. Dupré, R. B. Cal, and M. Calaf, "Pathways for mitigating thermal losses in solar photovoltaics," *Sci. Rep.*, vol. 8, no. 1, Dec. 2018, Art. no. 13163, doi: 10.1038/s41598-018-31257-0.
- [10] G. Perrakis *et al.*, "Passive radiative cooling and other photonic approaches for the temperature control of photovoltaics: A comparative study for crystalline silicon-based architectures," *Opt. Exp.*, vol. 28, no. 13, pp. 18548–18565, Jun. 2020, doi: 10.1364/OE.388208.
- [11] M. Muller, B. Marion, and J. Rodriguez, "Evaluating the IEC 61215 Ed.3 NMOT procedure against the existing NOCT procedure with PV modules in a side-by-side configuration," in *Proc. IEEE 38th Photovolt.* Specialist Conf., 2012, pp. 000697–000702, doi: 10.1109/PVSC.2012. 6317705
- [12] M. A. Goforth, G. W. Gilchrist, and J. D. Sirianni, "Cloud effects on thermal downwelling sky radiance," in *Proc. Thermosense XXIV*, Mar. 2002, pp. 203–213. doi: 10.1117/12.459570.
- [13] A. Wheeler, M. Leveille, I. Anton, M. Limpinsel, and S. Kurtz, "Outdoor performance of PV technologies in simulated automotive environments," in *Proc. IEEE 46th Photovolt. Specialist Conf.*, Jun. 2019, pp. 3103–3110, doi: 10.1109/PVSC40753.2019.8981352.
- [14] N. H. Reich et al., "Performance ratio revisited: Is PR >90% realistic?," Prog. Photovolt., vol. 20, no. 6, pp. 717–726, 2012, doi: 10.1002/pip.1219.
- [15] National Renewable Energy Laboratory. Reference Solar Spectral Irradiance: Air Mass 1.5, ASTM G-173-03, 2012. [Online]. Available: http://rredc.nrel.gov/solar/spectra/am1.5/
- [16] I. Subedi, T. J. Silverman, M. G. Deceglie, and N. J. Podraza, "PERC silicon PV infrared to ultraviolet optical model," Sol. Energy Mater Sol. Cells, vol. 215, Sep. 2020, Art. no. 110655, doi: 10.1016/j.solmat.2020. 110655.
- [17] M. Hammami, S. Torretti, F. Grimaccia, and G. Grandi, "Thermal and performance analysis of a photovoltaic module with an integrated energy storage system," *Appl. Sci.*, vol. 7, no. 11, Nov. 2017, Art. no. 11, doi: 10.3390/app7111107.
- [18] E. M. Sparrow, J. W. Ramsey, and E. A. Mass, "Effect of finite width on heat transfer and fluid flow about an inclined rectangular plate," *J. Heat Transfer – T ASME*, vol. 101, no. 2, pp. 199–204, May 1979 doi: 10.1115/1.3450946.
- [19] J. Watmuff, W. Charters, and D. Proctor, "Solar and wind induced external coefficients - Solar collectors," 2nd Revue Internationale d'Heliotechnique, p. 56, Jun. 1977.
- [20] R. J. Cole and N. S. Sturrock, "The convective heat exchange at the external surface of buildings," *Building Environ.*, vol. 12, no. 4, pp. 207–214, Jan. 1977, doi: 10.1016/0360-1323(77)90021-X.
- [21] A. Goetzberger, "Optical confinement in thin Si-solar cells by diffuse back reflectors," in *Proc. IEEE 15th Photovolt. Specialist Conf.*, 1981, pp. 867–870.
- [22] J. M. Gee, "The effect of parasitic absorption losses on light trapping in thin silicon solar cells," in *Proc. IEEE 20th Photovolt. Specialist Conf.*, 1988, pp. 549–554, doi: 10.1109/PVSC.1988.105762.

[23] Z. C. Holman et al., "Parasitic absorption in the rear reflector of a silicon solar cell: Simulation and measurement of the sub-bandgap reflectance for common dielectric/metal reflectors," Sol. Energy Mater Sol. Cells, vol. 120, pp. 426–430, Jan. 2014, doi: 10.1016/j.solmat.2013.06.024.

- [24] M. Vogt, "Development of physical models for the simulation of optical properties of solar cell modules," Ph.D. dissertation, Dept. Phys., TU Delft, Delft, The Netherlands, 2015, doi: 10.15488/8592.
- [25] M. Rüdiger, J. Greulich, A. Richter, and M. Hermle, "Parameterization of free carrier absorption in highly doped silicon for solar cells," *IEEE Trans. Electron. Devices*, vol. 60, no. 7, pp. 2156–2163, Jul. 2013, doi: 10.1109/TED.2013.2262526.
- [26] P. Uprety, I. Subedi, M. Junda, R. Collins, and N. Podraza, "Photogenerated carrier transport properties in silicon photovoltaics," *Sci. Rep.*, vol. 9, Dec. 2019, Art. no. 19015, doi 10.1038/s41598-019-55173-z.
- [27] B. Min et al., "A roadmap toward 24% efficient PERC solar cells in industrial mass production," *IEEE J. Photovolt.*, vol. 7, no. 6, pp. 1541–1550, Nov. 2017, doi: 10.1109/JPHOTOV.2017.2749007.
- [28] M. A. Green, "Lambertian light trapping in textured solar cells and light-emitting diodes: Analytical solutions," *Prog. Photovolt.*, vol. 10, no. 4, pp. 235–241, Jun. 2002, doi: 10.1002/pip.404.
- [29] E. Yablonovitch, "Statistical ray optics," J. Opt. Soc. Amer., vol. 72, no. 7, pp. 899–907, Jul. 1982, doi: 10.1364/JOSA.72.000899.
- [30] I. M. Slauch, M. G. Deceglie, T. J. Silverman, and V. E. Ferry, "Optical approaches for passive thermal management in c-Si photovoltaic modules," *Cell Rep. Phys. Sci.*, vol. 2, no. 5, May 2021, Art. no. 100430, doi: 10.1016/j.xcrp.2021.100430.
- [31] P. A. Basore, "Extended spectral analysis of internal quantum efficiency," in *Proc. IEEE 38th Photovolt. Specialist Conf.*, 1993, pp. 147–152. doi: 10.1109/PVSC.1993.347063.
- [32] J. Müller, S. Gatz, and R. Brendel, "Optimizing the geometry of local aluminum-alloyed contacts to fully screen-printed silicon solar cells," in Proc. IEEE 15th Photovolt. Specialist Conf., 2012, pp. 002223–002228.
- [33] T. Dullweber, "High-Efficiency industrial PERC solar cells for monofacial and bifacial applications," in *High-Efficient Low-Cost Photo-voltaics: Recent Developments*, V. Petrova-Koch, R. Hezel, and A. Goetzberger, Eds., Berlin, Germany: Springer-Verlag, 2009, pp. 65–94, doi: 10.1007/978-3-540-79359-5.
- [34] G. Perrakis et al., "Combined nano and micro structuring for enhanced radiative cooling and efficiency of photovoltaic cells," Sci. Rep., vol. 11, no. 1, Dec. 2021, Art. no. 11552, doi: 10.1038/s41598-021-91061-1.
- [35] A. Riverola et al., "Mid-infrared emissivity of crystalline silicon solar cells," Sol. Energy Mater Sol. Cells, vol. 174, pp. 607–615, Jan. 2018, doi: 10.1016/j.solmat.2017.10.002.
- [36] S. Kurtz et al., "Evaluation of high-temperature exposure of photovoltaic modules," Prog. Photovolt., Res. Appl., vol. 19, no. 8, pp. 954–965, 2011, doi: 10.1002/pip.1103.
- [37] N. C. Park, W. W. Oh, and D. H. Kim, "Effect of temperature and humidity on the degradation rate of multicrystalline silicon photovoltaic module," *Int. J. Photoenergy*, vol. 2013, pp. 1–9, 2013, doi: 10.1155/2013/925280.
 [38] L. Xu *et al.*, "Heat generation and mitigation in silicon solar
- [38] L. Xu *et al.*, "Heat generation and mitigation in silicon solar cells and modules," *Joule*, vol. 5, no. 3, pp. 631–645, Mar. 2021, doi: 10.1016/j.joule.2021.01.012.
- [39] A. Pfreundt et al., "Post-processing thickness variation of PV module materials and its impact on temperature, mechanical stress and power," in Proc. 36th Eur. Photovolt. Sol. Energy Conf. Exhib., Marseille, France, 2019
- [40] M. Mittag et al., "TPedge: Qualification of a gas-filled, encapsulation-free glass-glass photovoltaic module.," in Proc. 30th Eur. Photovolt. Sol. Energy Conf. Exhib., Hamburg, Germany, 2015, doi: 10.4229/EU-PVSEC20152015-1CO.11.4.
- [41] A. Shamim, M. Noman, M. Zubair, A. D. Khan, and S. Saher, "A facile approach to determine the unknown refractive index (n) and extinction coefficient (k) of novel encapsulant materials used in back contact PV modules," *Appl. Phys. A*, vol. 124, no. 8, p. 542, Aug. 2018, doi: 10.1007/s00339-018-1974-x.
- [42] W. Li, Y. Shi, K. Chen, L. Zhu, and S. Fan, "A comprehensive photonic approach for solar cell cooling," ACS Photon., vol. 4, no. 4, pp. 774–782, Apr. 2017, doi: 10.1021/acsphotonics.7b00089.
- [43] I. M. Slauch, M. G. Deceglie, T. J. Silverman, and V. E. Ferry, "Model for characterization and optimization of spectrally selective structures to reduce the operating temperature and improve the energy yield of photovoltaic modules," ACS Appl. Energy Mater., vol. 2, no. 5, pp. 3614–3623, May 2019, doi: 10.1021/acsaem.9b00347.
- [44] X. Yu, Y. Qin, and Q. Peng, "Probe decomposition of methylammonium lead iodide perovskite in N₂ and O₂ by in situ infrared spectroscopy," *J. Phys. Chem. A*, vol. 121, no. 6, pp. 1169–1174, Feb. 2017, doi: 10.1021/acs.jpca.6b12170.